International Journal for Multiscale Computational Engineering, 6(5)393–410(2008)

Multiscale Modeling of Material Failure: From Atomic Bonds to Elasticity with Energy Limiters

K. Y. Volokh

Faculty of Civil and Environmental Engineering, Technion-Israel Institute of Technology, Haifa 32000, Israel

ABSTRACT

Separation of two particles is characterized by a magnitude of the bond energy, which limits the accumulated energy of the particle interaction. In the case of a solid comprising many particles, there exist a magnitude of the average bond energy, the failure energy, which limits the energy that can be accumulated in an infinitesimal material volume under strain. The energy limiter controls material softening; the softening indicates failure. Thus, by limiting the stored energy density, we include a description of material failure in the constitutive model. When the failure energy, that is, the energy limiter, is introduced in the constitutive model, it can be calibrated in macroscopic experiments. Traditional material models do not have energy limiters, and they allow for unlimited energy accumulation under the strain increase, which is unphysical because no material can sustain large enough strains without failure. We review the applications of the new approach based on the use of the energy limiters to failure of soft biological tissues and fracture of brittle materials. In addition, we consider new developments concerning the rate-dependent failure in solids and the drop of viscosity in fluids.

KEYWORDS

multiscale modeling, material failure, bonds, elasticity, energy limiters, softening

*Address all correspondence to cvolokh@technion.ac.il, Phone +972-48292426

1. INTRODUCTION

The problem of modeling the failure nucleation and propagation in solids is still largely open, despite the enormous progress in computational materials science and engineering during the past decades. Existing methods are too restrictive and computationally involved to be finally accepted as an optimal approach to modeling failure. For example, molecular dynamic simulations are restricted by length and timescales to such a degree that no real macroscopic materials and structures can be practically analyzed. On the other hand, continuum models that can handle macroscopic length- and timescales are phenomenological, and their experimental calibration is far from trivial; moreover, they are sophisticated mathematically and computationally.

The existing continuum models of material failure can be divided into two groups: surface and bulk models. The surface models, pioneered by Barenblatt [1], appear by the name of cohesive zone models (CZMs) in the modern literature. They present material surfaces—cohesive zones—where displacement discontinuities occur. The discontinuities are enhanced with constitutive laws relating normal and tangential displacement jumps with the corresponding tractions. There are plenty of proposals of constitutive equations for the cohesive zones (e.g., [2–6]). All CZMs are constructed qualitatively as follows: tractions increase, reach a maximum, and then approach zero with increasing separation. Such a scenario is in harmony with our intuitive understanding of the rupture process. Since the work by Needleman [7], CZMs are used increasingly in finite element simulations of crack tip plasticity and creep; crazing in polymers; adhesively bonded joints; interface cracks in bimaterials; delamination in composites and multilayers; fast crack propagation in polymers, and so on. Cohesive zones can be inside finite elements or along their boundaries [5, 8, 9]. Crack nucleation, propagation, branching, kinking, and arrest are a natural outcome of the computations where the discontinuity surfaces are spread over the bulk material. This is in contrast to the traditional approach of fracture mechanics, where stress analysis is separated from a description of the actual process of material failure. The CZM approach is natural for simulation of fracture at the internal material interfaces in polycrystals, composites, and multilayers. It is less natural for modeling fracture of the bulk because it leads to the simultaneous use of two material models for the same real material: one model describes the bulk, while the other model describes CZM imbedded in the bulk. Such a two-model approach is rather artificial physically. It seems preferable to incorporate a material failure law directly in the constitutive description of the bulk. Remarkably, the first models of bulk failure—damage mechanics—proposed by Kachanov and Rabotnov [10, 11] for analysis of the gradual failure accumulation and propagation in creep and fatigue appeared almost simultaneously with the cohesive zone approach. The need to describe the failure accumulation, that is, evolution of the material microstructure, explains why damage mechanics is very similar to plasticity theories, including (1) the internal damage variable (inelastic strain), (2) the critical threshold condition (yield surface), and (3) the damage evolution equation (flow rule). The subsequent development of the formalism of damage mechanics [12–15] left its physical origin well behind the mathematical and computational techniques and, eventually, led to the use of damage mechanics for the description of any bulk failure. Theoretically, the approach of damage mechanics is very flexible and allows reflecting physical processes, triggering macroscopic damage at small length scales. Practically, the experimental calibration of damage theories is hardly accessible because to measure the damage parameter directly is easier said than done. Moreover, the experimental calibration should include both the damage evolution equation and criticality condition.

A physically motivated multiscale alternative to damage mechanics in the cases of failure related with the bond rupture has been considered by Gao and Klein [16, 17], who showed how to mix the atomic/particulate and continuum descriptions to simulate material failure. They applied the Cauchy-Born rule, linking micro- and macroscales to empirical potentials, which include a possibility of the full atomic separation. The continuum-atomistic link led to the formulation of the macroscopic strain energy potentials, allowing for stress-strain softening and strain localization. The continuum-atomistic method is effective at small length scales, where purely atomistic analysis becomes computationally intensive. Unfortunately, a direct use of the continuum-atomistic method in macroscopic failure

problems is not very feasible because its computer implementation includes a numerically involved procedure of the averaging of the interatomic potentials over a representative volume.

To bypass the computational intensity of the continuum-atomistic method, while preserving its sound physical basis, the approach of energy limiters was proposed by Volokh [18–20]. The basic idea of the approach is to formulate expressions of the stored energy density, which include the energy limiter(s) – the failure energy. Such limiters induce strain softening, which is a material failure description, in the constitutive law. The energy limiter approach is computationally simple yet physically appealing, and we review and develop it in the present work.

2. MULTISCALE LINK: ENERGY LIMITERS

In this section, we show how the critical concept of the macroscopic stored energy limiter can be qualitatively derived from the microscopic considerations of the particle bonding.

We start with a consideration of the interaction of two particles by choosing, to be specific, the Lennard-Jones (LJ) potential:

$$\varphi(l) = 4\varepsilon\frac{\sigma^{12}}{l^{12}} - 4\varepsilon\frac{\sigma^{6}}{l^{6}} \tag{2.1}$$

where l is the distance between particles and ε and σ are the bond energy and length constants, respectively (Fig. 1).

Let L designate the distance between particles in a reference state and F be the one-dimensional deformation gradient. In the latter case, we have

$$l = FL \tag{2.2}$$

Substituting Eq. (2.2) into Eq. (2.1), we have

$$\varphi(F) = 4\varepsilon\frac{\sigma^{12}}{(FL)^{12}} - 4\varepsilon\frac{\sigma^{6}}{(FL)^{6}} \tag{2.3}$$

Assuming that deformation increases to infinity, we have

$$\varphi(F \to \infty) = 0 \tag{2.4}$$

On the other hand, we have at the reference state

$$\varphi_0 = \varphi(F = 1) = 4\varepsilon\frac{\sigma^{12}}{L^{12}} - 4\varepsilon\frac{\sigma^{6}}{L^{6}} \tag{2.5}$$

In the absence of external loads, the energy of the interaction tends to minimum, and it is natural to choose the minimum energy state – equilibrium – at distance $L = \sqrt[6]{2}\sigma$, where no forces are acting between the particles. In the latter case, we have

$$\varphi_0 = -\varepsilon \tag{2.6}$$

We notice that energy is negative in the equilibrium state according to the classical LJ potential. The latter is inconvenient in solid mechanics, and we modify the classical LJ potential by shifting its reference energy to zero (Fig. 1):

$$\psi = \varphi + \varepsilon \tag{2.7}$$

We further formalize the described energy shift as follows:

$$\psi(F) = \varphi(F) - \varphi_0 \tag{2.8}$$

$$\varphi_0 = \min_L \varphi(F = 1) \tag{2.9}$$

Equations (2.8) and (2.9) are essential in the subsequent consideration of assemblies of many particles.

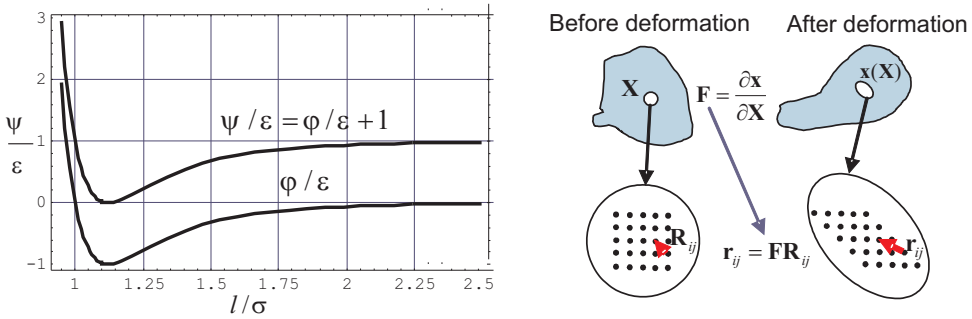

FIGURE 1. Lennard-Jones potential (left) and Cauchy-Born rule (right)

It is crucial to notice that we cannot increase energy in an unlimited manner by increasing deformation. The energy increase is limited:

$$\psi(F \to \infty) = -\varphi_0 = \Phi = \text{constant} \tag{2.10}$$

Now we extend all considerations for the pair of particles given previously to large assemblies of particles comprising solid bodies. We consider particles placed at $\mathbf{r}_i$ in the 3-D space. Generally, the volumetric density of the total potential energy, that is, the strain energy, can be written with an account of two-particle interactions, as follows:

$$\bar{\varphi} = \frac{1}{2V}\sum_{i,j}\varphi(r_{ij}) \tag{2.11}$$

where $r_{ij} = |\mathbf{r}_{ij}| = |\mathbf{r}_i - \mathbf{r}_j|$ and V is the volume occupied by the system.

According to the Cauchy-Born rule [21, 22]; originally applied to the crystal elasticity, the current $\mathbf{r}_{ij}$ and initial (reference) $\mathbf{R}_{ij} = \mathbf{R}_i - \mathbf{R}_j$ relative positions of two particles can be related by linear mapping.

$$\mathbf{r}_{ij} = \mathbf{F}\mathbf{R}_{ij} \tag{2.12}$$

where $\mathbf{F} = \partial\mathbf{x}/\partial\mathbf{X}$ is the deformation gradient of a generic continuum particle of body Ω occupying position $\mathbf{X}$ at the reference state and position $\mathbf{x}(\mathbf{X})$ at the current state of deformation (Fig. 1).

Substituting Eq. (2.12) into Eq. (2.11) yields

$$\bar{\varphi} = \frac{1}{2V}\sum_{i,j}\varphi(r_{ij}) = \frac{1}{2V}\sum_{i,j}\varphi(r_{ij}(\mathbf{C})) \tag{2.13}$$

where $\mathbf{C} = \mathbf{F}^T\mathbf{F}$ is the right Cauchy-Green tensor.

Direct application of Eq. (2.13) to the analysis of material behavior can be difficult because of the large amount of particles. Gao and Klein [16, 17] considered the following statistical averaging procedure:

$$\langle\varphi(l)\rangle = \frac{1}{V_0}\int_{V_0^*}\varphi(l)D_V dV \tag{2.14}$$

$$l = r_{ij} = L\sqrt{\xi\cdot\mathbf{C}\xi} = L\,|\mathbf{F}\xi| \tag{2.15}$$

where $L = R_{ij} = |\mathbf{R}_i - \mathbf{R}_j|$ is the reference bond length; $\xi = (\mathbf{R}_i - \mathbf{R}_j)/L$ is the reference bond direction; V_0 is the reference representative volume; $\varphi(l)$ is the bond potential (LJ); D_V is the volumetric bond density function; and V_0^* is the integration volume defined by the range of influence of φ. The reader is advised to consult [23] for examples of the bond density functions.

Now the average strain energy takes the form

$$\langle\varphi(\mathbf{C})\rangle = \frac{1}{V_0}\int_{V_0^*}4\varepsilon\left[\frac{\sigma^{12}}{L^{12}\|\mathbf{C}\|^{12}} - \frac{\sigma^6}{L^6\|\mathbf{C}\|^6}\right]D_V dV \tag{2.16}$$

where

$$\|\mathbf{C}\| = \sqrt{\xi\cdot\mathbf{C}\xi} \tag{2.17}$$

Analogously to the case of the pair interaction considered in the previous subsection (Eqs. (2.8) and (2.9)), we define the shifted strain energy, which is zero at the equilibrium reference state, as

$$\psi(\mathbf{C}) = \langle\varphi(\mathbf{C})\rangle - \langle\varphi\rangle_0 \tag{2.18}$$

$$\langle\varphi\rangle_0 = \min_L\langle\varphi(\mathbf{C}=\mathbf{1})\rangle \tag{2.19}$$

Analogously to Eq. (2.10), we can define the average bond energy or the failure energy by setting an unlimited increase of deformation:

$$\Phi = \psi(\|\mathbf{C}\| \to \infty) = -\langle\varphi\rangle_0 = \text{constant} \tag{2.20}$$

Thus the average bond energy sets a limit for the energy accumulation. This conclusion generally does not depend on the choice of the particle potential, and it is valid for any interaction that includes a possible particle separation (the bond energy).

Contrary to the preceding conclusion, traditional hyperelastic models of materials do not include the energy limiter. The stored energy of hyperelastic materials is defined as

$$\psi = W \tag{2.21}$$

Here W is used for the strain energy of the *intact* material, which can be characterized as follows:

$$\|\mathbf{C}\| \to \infty \Rightarrow \psi = W \to \infty \tag{2.22}$$

where $\|...\|$ is a tensorial norm.

In other words, the increasing strain increases the accumulated energy in an unlimited manner. Evidently, the consideration of only intact materials is restrictive and unphysical. The energy increase of a real material should be limited, as was shown previously:

$$\|\mathbf{C}\| \to \infty \Rightarrow \psi \to \Phi = \text{constant} \tag{2.23}$$

where the average bond energy, $\Phi = \text{constant}$, can be called the material failure energy.

Equation (2.23) presents the fundamental idea of introducing a limiter of the stored energy in the elasticity theory. Such a limiter induces material softening, indicating material failure, automatically. The choice of the limited stored energy expression should generally be material- or problem-specific. Nonetheless, a somewhat general ("try first") formula [20] can be introduced to enrich the already existing models of intact materials with the failure description

$$\psi(W) = \Phi - \Phi \exp\left[-\frac{W}{\Phi}\right] \tag{2.24}$$

where $\psi(W=0)=0$ and $\psi(W=\infty)=\Phi$.

Equation (2.24) obeys condition $\|\mathbf{C}\| \to \infty \Rightarrow \psi(W(\mathbf{C})) \to \Phi$, and in the case of the intact material behavior, $W \ll \Phi$, we have $\psi(W) \approx W$ preserving the features of the intact material.

We strongly emphasize, however, that although Eq. (2.24) is somewhat general, it should not be considered as a panacea; rather, the introduction of the energy limiters should be material- or problem-specific. Various ways of introducing the energy limiters are considered later.

Remark 2.1. The so-called Cauchy-Born rule linking micro- and macroscales was originally formulated for crystal elasticity, and it is widely used in modern continuum-atomistic methods. The Cauchy-Born rule is essentially an assumption of affinity of deformation of the physical particles within the representative small volumes of material. The applicability of the affinity hypothesis implies the applicability of the classical (local) continuum mechanics description of material. The continuum description of material proved itself for most materials at large length scales. It may fail, however, at small length scales, where, for example, the atomic relaxation cannot be ignored. The latter cases are out of our consideration, and we always assume that the local deformation is approximately affine.

Remark 2.2. It is important to realize that not all bonds between the material particles are of equal importance in Eq. (2.14). Only bonds presenting the weakest links control failure. In this sense, it is probably better to call the energy limiter the failure energy, rather than the average bond energy.

3. FAILURE OF SOFT BIOLOGICAL TISSUES

We consider applications of energy limiters to analysis of failure of soft biological tissues.

The first example clarifying the meaning of the method and the ways of experimental calibration involves the material of the abdominal aortic aneurism (AAA). AAA is a focal dilation of the infrarenal aorta found in $\approx 2\%$ of the elderly population, with $\approx 150,000$ new cases diagnosed each year – and the occurrence is increasing. In many cases, AAA gradually expands until rupture, causing a mortality rate of 90%. Volokh and Vorp [24] proposed the following analytical model of the incompressible AAA material accounting for failure:

$$\psi(I_1) = \Phi - \Phi \exp\left[-\frac{\alpha_1}{\Phi}(I_1-3) - \frac{\alpha_2}{\Phi}(I_1-3)^2\right] \tag{3.1}$$

where $I_1 = \operatorname{tr}\mathbf{C}$, α_1 and α_2 are the elasticity constants of the material, and Φ is the failure energy.

The constitutive law for the Cauchy stress, $\boldsymbol{\sigma}$, is obtained from Eq. (3.1), as follows:

$$\sigma = -p\mathbf{1} + 2\psi_1 \mathbf{B} \tag{3.2}$$

where $\mathbf{B} = \mathbf{F}\mathbf{F}^T$ is the left Cauchy-Green tensor; p is the Lagrange multiplier enforcing the incompressibility condition, and

$$\psi_1 \equiv \frac{\partial \psi}{\partial I_1} = [\alpha_1 + 2\alpha_2(I_1-3)] \exp\left[-\frac{\alpha_1}{\Phi}(I_1-3) - \frac{\alpha_2}{\Phi}(I_1-3)^2\right] \tag{3.3}$$

The uniaxial tension test results are shown in Fig. 2, where Eq. (3.1) is calibrated with the follow-

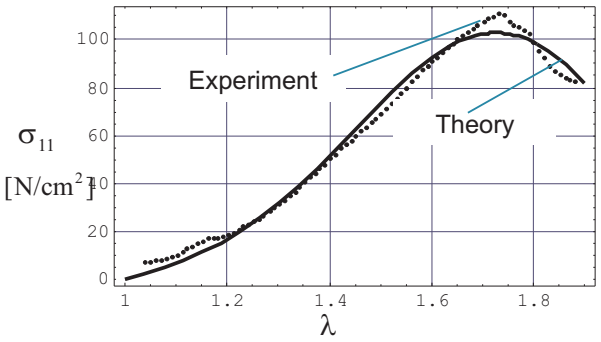

FIGURE 2. Theory versus experiment for the uniaxial tension test of abdominal aortic aneurism (AAA) [24]

ing constants: $\alpha_1 = 10.3\ \mathrm{N/cm^2}$, $\alpha_2 = 18.0\ \mathrm{N/cm^2}$ and $\Phi = 40.2\ \mathrm{N/cm^2}$.

The maximum point on the curve in Fig. 2 corresponds to the onset of static instability (failure). The intact material model of AAA corresponding to Eq. (3.1) is $W(I_1) = \alpha_1(I_1 - 3) + \alpha_2(I_1 - 3)^2$, which does not include a failure description. It was experimentally validated in [25]. Though the authors presented experimental data on postfailure, their model was only fit to the prefailure data. We refer to [24] for further details of the use of energy limiters for the prediction of AAA rupture and turn to the next example.

The objective of the second example was to clarify the effect of residual strains on the overall strength of arteries [26]. Residual stresses and strains are accumulated during growth in arteries and, generally, in soft biological tissues, and they present one of the most intriguing features of the mechanics of living soft materials [27–29]. Fung [30] suggested the following deformation law to account for residual strains in the artery, which is considered as an infinite incompressible cylinder inflating in the radial direction:

$$r = \sqrt{\frac{R^2 - A^2}{\gamma\, s} + a^2}, \quad \theta = \gamma\Theta, \quad z = sZ \tag{3.4}$$

where a point occupying position (R, Θ, Z) in the reference configuration is moving to position (r, θ, z) in the current configuration; s is the axial stretch; $\gamma = 2\pi/(2\pi - \omega)$, where ω is the artery opening angle in the reference configuration (Fig. 3); and

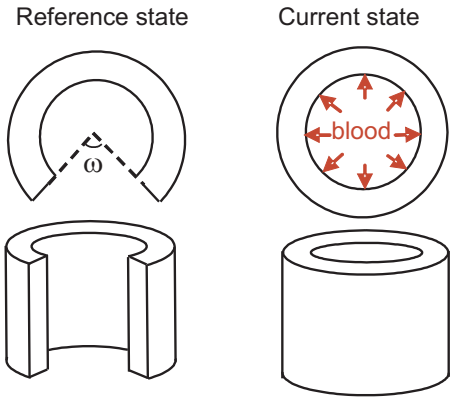

FIGURE 3. Residual stresses in arteries with the opening angle ω in the reference state

A and a are the internal artery radii before and after deformation, respectively.

Fung [31] used the following exponential stored energy function and constitutive law to analyze the artery inflation:

$$\begin{aligned} W &= \frac{c}{2}(e^Q - 1) \\ Q &= c_1 E_{RR}^2 + c_2 E_{\Theta\Theta}^2 + c_3 E_{ZZ}^2 + 2c_4 E_{RR} E_{\Theta\Theta} \\ &\quad + 2c_5 E_{ZZ} E_{\Theta\Theta} + 2c_6 E_{RR} E_{ZZ} \end{aligned} \tag{3.5}$$

$$\boldsymbol{\sigma} = -p\mathbf{1} + \mathbf{F}\frac{\partial W}{\partial \mathbf{E}}\mathbf{F}^T \tag{3.6}$$

where the components of the Green strain, $\mathbf{E} = (\mathbf{C} - \mathbf{1})/2$, have been used and material constants were experimentally calibrated for a carotid artery: $c_1 = 0.0089$, $c_2 = 0.9925$, $c_3 = 0.4180$, $c_4 = 0.0193$, $c_5 = 0.0749$, and $c_6 = 0.0295$.

In the case of a strain-free reference state with $\omega = 0^\circ$ and the internal and external reference radii $A = 0.71$ mm and $B = 1.10$ mm, respectively, the pressure radius and stress distribution curves are calculated and presented in Fig. 4. The stresses, $\bar{\sigma}_{ij} = \sigma_{ij}/c$, are presented for dimensionless pressure $\bar{g} = g/c = 0.5$, which corresponds to pressure $g = 13.47$ KPa for the shear modulus $c = 26.95$ KPa.

In the case of a prestrained state with $\omega = 160^\circ$ and the internal and external reference radii $A = 1.43$ mm and $B = 1.82$ mm, respectively, the pressure radius and stress distribution curves are presented in Fig. 5. The stresses are presented for dimensionless pressure $\bar{g} = 0.5$, which corresponds to pressure $g = 13.47$ KPa for the shear modulus $c = 26.95$ KPa.

We note that the pressure increase always corresponds to the radius increase; that is, the artery deformation is always stable and no failure is observed. The latter is unphysical, of course, and a failure description should be included in the constitutive setting and observed on the pressure radius curve as an onset of instability. Such account of the artery failure can be done by using energy limiters [26]. In the latter case, it is possible to replace Eqs. (3.5) and (3.6) of the intact artery with the following model of artery with failure:

$$\psi = \Phi - \Phi \exp\left[-\frac{W}{\Phi}\right] \tag{3.7}$$

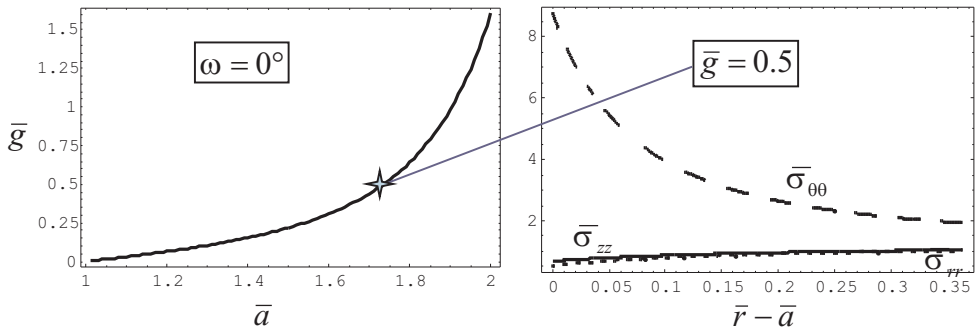

FIGURE 4. Pressure radius (left) and true stress (right) curves for artery without prestrain

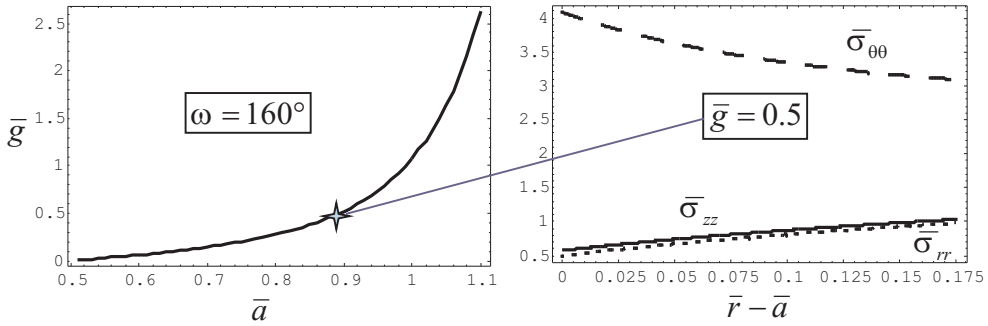

FIGURE 5. Pressure radius (left) and true stress (right) curves for artery with prestrain

$$\boldsymbol{\sigma} = -p\mathbf{1} + \mathbf{F}\frac{\partial \psi}{\partial \mathbf{E}}\mathbf{F}^T \tag{3.8}$$

where W has been defined in Eq. (3.5).

We repeat the analyses shown in Figs. 4 and 5 by using Eqs. (3.7)–(3.8) for $\bar{\Phi} = \Phi/c = 1$ and present the results in Fig. 6.

We note that failure appears on the pressure radius curve as a limit point where static instability occurs. Though the decreasing branch of the curve is shown for the sake of consistency, it should be clearly realized that it is not statically stable, and the dynamic failure propagation should be generally monitored after the limit point. It can be noticed that residual strain can increase the overall arterial strength significantly. The preexisting compressive strains in arteries delay the onset of rupture like the preexisting compression in the prestressed concrete delays the crack opening. It is also interesting that the prestrain makes the distribution of the hoop stresses more uniform. In a sense, the prestrain optimizes the stress distribution in a loaded artery.

Proceeding with the artery analysis, we turn to the third example, illustrating the capability of the energy limiters to handle more sophisticated material models. Particularly, we consider the arterial wall to be a fiber-reinforced composite including the inner layer of media and the outer layer of adventitia. Every layer is described by the following constitutive law:

$$\boldsymbol{\sigma} = -p\mathbf{1} + 2\psi_1\mathbf{B} + 2\varsigma_1\mathbf{m}_1 \otimes \mathbf{m}_1 + 2\varsigma_2\mathbf{m}_2 \otimes \mathbf{m}_2 \tag{3.9}$$

$$\psi_1 = \frac{c}{2}\exp\left[-\frac{c}{2\Phi}(I_1 - 3)\right] \tag{3.10}$$

$$\varsigma_i = k_1(J_i - 1)\exp\left[k_2(J_i - 1)^2 - k_2\frac{(J_i - 1)^{2n_i}}{(\xi_i^2 - 1)^{2n_i}}\right] \tag{3.11}$$

where the second term on the right-hand side of Eq. (3.9) describes the media/adventitia matrix with $I_1 = \text{tr}\mathbf{B} = \text{tr}\mathbf{C}$, while the third and the fourth terms on the right-hand side of Eq. (3.9) describe two families of collagen fibers with vectors $\mathbf{m}_i = \mathbf{F}\mathbf{M}_i$ designating "pushed-forward" initial fiber directions $\mathbf{M}_i$ ($|\mathbf{M}_i| = 1$) and $J_i = \mathbf{m}_i \cdot \mathbf{m}_i$. Constants of intact ma-

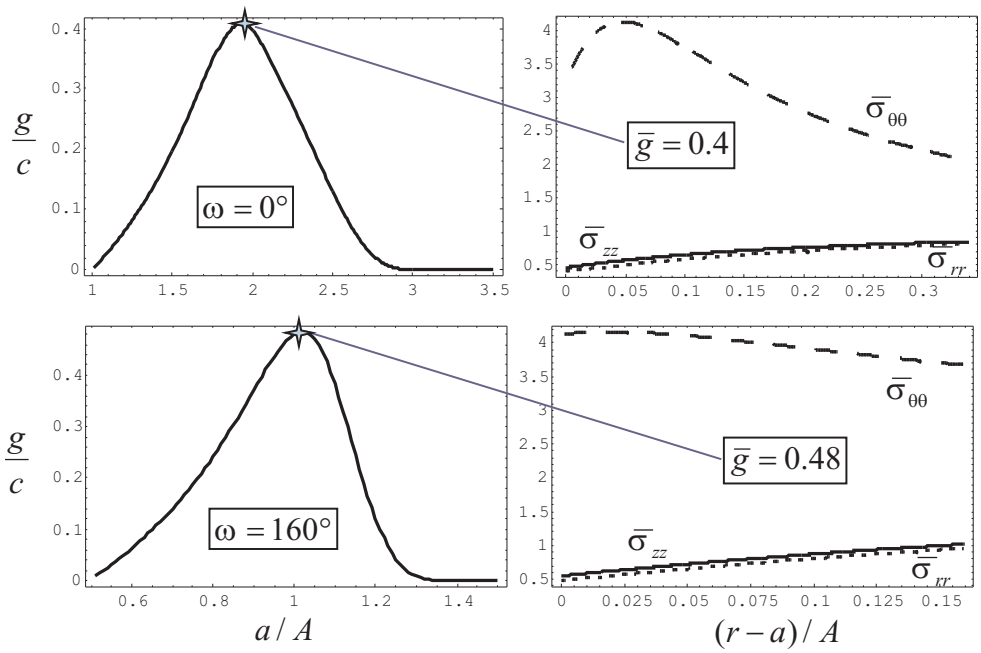

FIGURE 6. Pressure radius (left) and true stress (right) curves for $\bar{\Phi} = \Phi/c = 1$ without and with prestrain accounting for material failure

terials (c and k_i) are completed with constants describing failure (Φ, ξ_i, n_i).

The stress-stretch curves for matrix and fibers with and without failure are presented in Fig. 7 for the case of uniaxial tension.

Applying the constitutive law of Eqs. (3.9)–(3.11) to the considered example of the arterial inflation, it is possible to calculate the pressure radius curve shown in Fig. 8 for the following parameters of the media: $c_M = 3.0$ [KPa], $k_{1M} = 2.36$ [KPa], $k_{2M} = 0.84$, $A = 1.43$ [mm], $B_M = 1.69$ [mm], $\beta_M = \pi/6$, $\Phi_M = c_M$, $\xi_{1M} = 1.5$, $n_{1M} = 10$; likewise, for adventitia, $c_A = 0.3$ [KPa], $k_{1A} = 0.56$ [KPa], $k_{2A} = 0.7112$, $A_A = B_M$, $B = 1.82$ [mm], $\beta_A = \pi/3$, $\Phi_A = c_A$, $\xi_{1A} = 1.7$, and $n_{1A} = 10$, where $\beta_{M(A)}$ is the angle between the fibers and the circumferential direction of the artery. In addition, we assume that $s = 1$ and $\omega = 160°$.

It is also interesting that by varying the parameters of failure, it is possible to get deeper insight into the role of matrix and fibers in the overall strength of arteries. The studies in [32] suggested the follow-

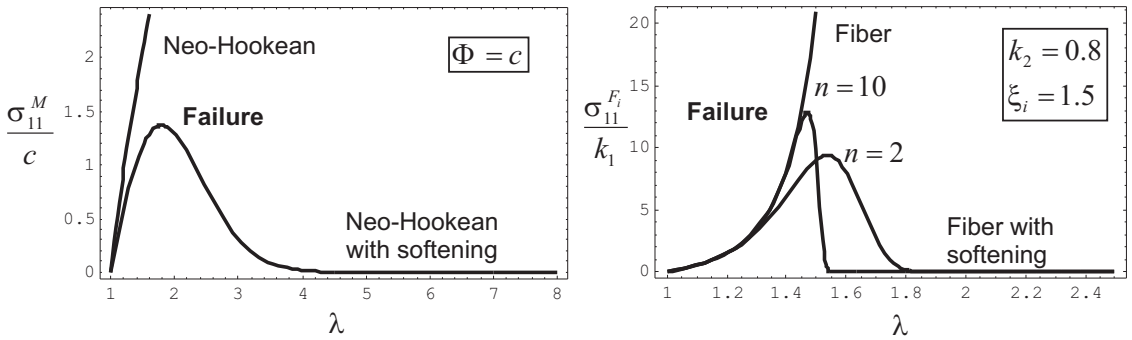

FIGURE 7. Matrix and fibers with and without softening in the case of uniaxial tension

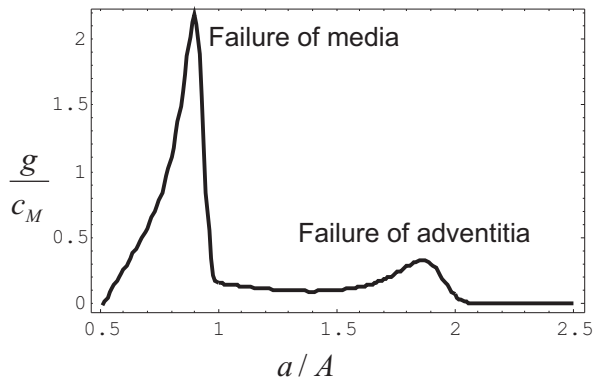

FIGURE 8. Pressure radius curve for the bilayer arterial wall with residual strains

ing conclusions: First, it was found that the fiber strength dominates the overall arterial strength; second, it was also found that the medium dominates the overall arterial strength and plays a crucial role in the load-bearing capacity of arteries; third, it was again found that residual strains can increase overall arterial strength significantly.

4. BRITTLE FRACTURE WITH ENERGY LIMITERS

In this section, we turn to another field of application of energy limiters, concerned with the fracture of brittle and quasibrittle materials.

Application of energy limiters to the analysis of the onset of the crack propagation [33, 34] was motivated by the following disagreement between theory and experiment: It was experimentally found that calibration of the material toughness in ceramics was significantly affected by the sharpness (tip radius) of a real crack. These experimental results were not entirely compatible with the original Griffith [35] theory of brittle fracture, where the crack sharpness was of minor influence. To shed more light on this disagreement between the experimental importance of the crack sharpness and its theoretical ignorance, we studied the Griffith problem computationally by using energy limiters for Hookean solids [33].

Two different models with the energy limiter for the Hookean solid have been used. The first model [18, 19] is described by the following constitutive law:

$$\psi = \Phi - \Phi \exp\left[-\frac{\lambda}{2\Phi}(\mathrm{tr}\boldsymbol{\varepsilon})^2 - \frac{\mu}{\Phi}\boldsymbol{\varepsilon}:\boldsymbol{\varepsilon}\right] \tag{4.1}$$

$$\boldsymbol{\sigma} = \frac{\partial \psi}{\partial \boldsymbol{\varepsilon}} = 2\tilde{\mu}\boldsymbol{\varepsilon} + \tilde{\lambda}(\mathrm{tr}\boldsymbol{\varepsilon})\mathbf{1} \tag{4.2}$$

$$\tilde{\mu} = \mu \exp\left[-\frac{\lambda}{2\Phi}(\mathrm{tr}\boldsymbol{\varepsilon})^2 - \frac{\mu}{\Phi}\boldsymbol{\varepsilon}:\boldsymbol{\varepsilon}\right] \tag{4.3}$$

$$\tilde{\lambda} = \lambda \exp\left[-\frac{\lambda}{2\Phi}(\mathrm{tr}\boldsymbol{\varepsilon})^2 - \frac{\mu}{\Phi}\boldsymbol{\varepsilon}:\boldsymbol{\varepsilon}\right] \tag{4.4}$$

where λ, μ are the Lame constants; $\boldsymbol{\varepsilon}:\boldsymbol{\varepsilon} = \mathrm{tr}(\boldsymbol{\varepsilon}\boldsymbol{\varepsilon}^T)$, $\boldsymbol{\varepsilon} = (\mathbf{H} + \mathbf{H}^T)/2$ is the linear strain; $\mathbf{H} = \partial\mathbf{u}/\partial\mathbf{X}$ is the displacement, $\mathbf{u} = \mathbf{x} - \mathbf{X}$ is the gradient; and $\mathbf{1}$ is the second-order identity tensor.

The second model is obtained from Eq. (2.24) for small deformations and leads to the following constitutive law:

$$\psi = \Phi - \Phi\left(1 + \sqrt{\frac{K}{\Phi}}\,\mathrm{tr}\boldsymbol{\varepsilon}\right)\exp\left[-\sqrt{\frac{K}{\Phi}}\mathrm{tr}\boldsymbol{\varepsilon} - \frac{\mu}{\Phi}\mathbf{e}:\mathbf{e}\right] \tag{4.5}$$

$$\boldsymbol{\sigma} = \frac{\partial \psi}{\partial \boldsymbol{\varepsilon}} = 2\tilde{\mu}\,\boldsymbol{\varepsilon} + \left(\tilde{K} - \frac{2}{3}\tilde{\mu}\right)(\mathrm{tr}\boldsymbol{\varepsilon})\mathbf{1} \tag{4.6}$$

$$\tilde{\mu} = \mu\left(1 + \sqrt{\frac{K}{\Phi}}\mathrm{tr}\boldsymbol{\varepsilon}\right)\exp\left[-\sqrt{\frac{K}{\Phi}}\mathrm{tr}\boldsymbol{\varepsilon} - \frac{\mu}{\Phi}\mathbf{e}:\mathbf{e}\right] \tag{4.7}$$

$$\tilde{K} = K \exp\left[-\sqrt{\frac{K}{\Phi}}\,\mathrm{tr}\boldsymbol{\varepsilon} - \frac{\mu}{\Phi}\,\mathbf{e}:\mathbf{e}\right] \tag{4.8}$$

where $K = \lambda + 2\mu/3$ is the bulk modulus and $\mathbf{e} = \boldsymbol{\varepsilon} - (\mathrm{tr}\boldsymbol{\varepsilon})1/3$ is the strain deviator.

Evidently, the Hooke law is derived from Eqs. (4.2) and (4.6) in the linearized case, where $\tilde{\mu} = \mu$, $\tilde{\lambda} = \lambda$, and $\tilde{K} = K$. The main physical difference between Eq. (4.2) and Eq. (4.6) is that the former allows for failure in hydrostatic compression, while the latter does not.

The introduced constitutive models of Eqs. (4.2) and Eq. (4.6) were plugged into ABAQUS finite element software, and the hydrostatic (biaxial) tension of a thin plate with *small* elliptic and straight cracks (Fig. 9) under the varying sharpness and length of the cracks was simulated.

The state of the plane stress for a square plate of size $d = 1600$ with elastic constants $\lambda/\Phi = 75{\cdot}10^4/66$ and $\mu/\Phi = 90{\cdot}10^4/66$ was considered, and very fine meshes were used, as shown, for example, in Fig. 10. The number of elements varied for various loading cases.

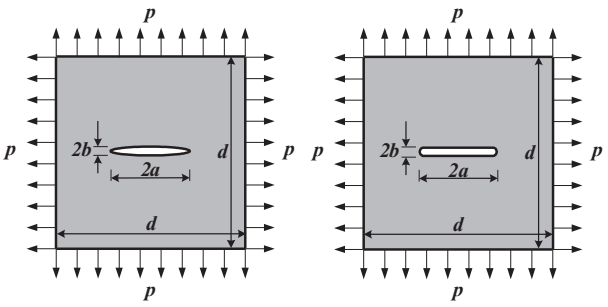

FIGURE 9. Elliptic and straight cracks under hydrostatic tension

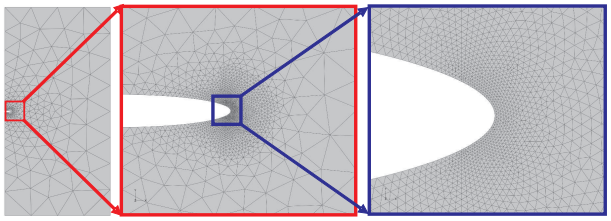

FIGURE 10. Sample finite element mesh for elliptic crack

Three series of simulations were performed [33]. First, the elliptic crack with a fixed length of $2a = 80$ and varying sharpness, that is, the width half axes of the elliptic crack, $b = 1, 2, 3, 4, 5, 6, 7, 8$, was analyzed. Figure 11 presents the normalized critical tension, where the onset of static instability occurs, versus varying crack sharpness.

It is clearly seen that the critical tension significantly depends on the sharpness of the elliptic crack. When the critical tension is known, it is possible to calculate the material toughness by using

$$K_{Ic} = p_{cr}\sqrt{\pi\, a} \tag{4.9}$$

Evidently, the material toughness depends linearly on the critical tension, and consequently, no unique toughness can be determined for a crack with a fixed length. The numerical value of the toughness depends on the sharpness of the crack. It is worth noting that the "smallness" of the crack was checked by comparing the results of the present computations to the results of the similar computations with the enlarged plate.

Qualitatively similar results are also obtained for the straight crack, which is formed by two parallel lines joined by half-circles at the edges. Figure 12 shows the critical tension for the case of the straight crack with varying sharpness, that is, width. Again, like in the case of the elliptic crack, no unique magnitude of the critical tension and, consequently, material toughness can be determined because it depends on the crack sharpness.

In addition to analysis of the influence of the crack sharpness on the critical tension of a plate, it was of interest to compare cracks with equivalent sharpness and varying lengths. Such comparisons are presented in Fig. 13. The obtained data clearly show that the crack length affects the critical tension in agreement with the Griffith theory only in the

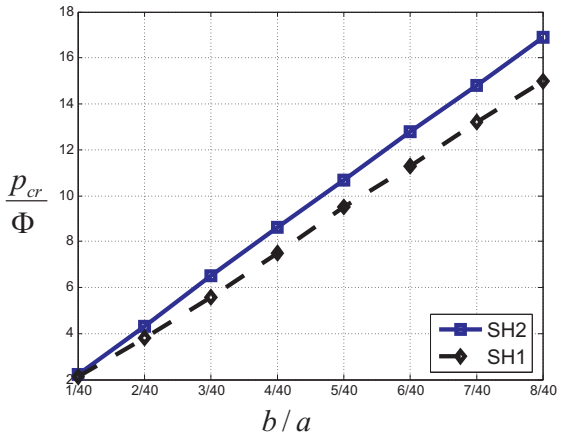

FIGURE 11. Critical tension for elliptic crack with varying sharpness and fixed length

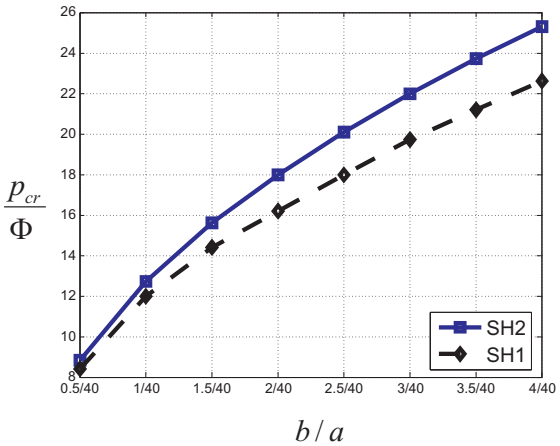

FIGURE 12. Critical tension for straight crack with varying sharpness and fixed length

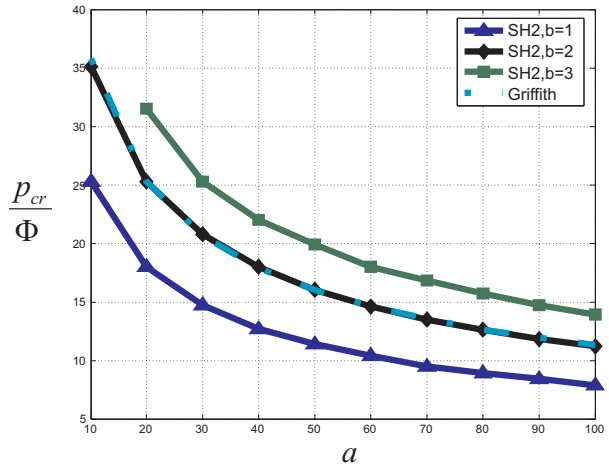

FIGURE 13. Critical tension for straight crack with fixed yet different sharpness and varying length (Griffith solution is given for at $a/b = 50/2$)

case of the cracks with equivalent sharpness. The latter means that if the Griffith theory was calibrated for the sharpness corresponding to the middle curve in Fig. 13, then it could only predict the behavior of the cracks with the same sharpness, and it would fail in predicting the behavior of cracks with a different sharpness.

The main practical implication of our results is a conclusion that generally, material toughness cannot be uniquely calibrated in experimental tests because its numerical magnitude significantly depends on the sharpness of the crack or notch used for the calibration. The crack sharpness controls the stress-strain concentration, which in turn controls the onset of fracture. It is possible, however, to decrease the radius of the tip of the crack or notch to a magnitude where our conclusion based on the classical continuum considerations is not applicable. Such a magnitude should be related to a characteristic length of the material microstructure, for example, grain size, atomic distance, and so on.

It should be noted that the interpretation of our results must be cautious. Though Griffith theory ignores the actual sharpness of the real physical cracks, the theory still has a predictive power in the following asymptotic sense: If a true material toughness can be found in experiments, then the Griffith theory can be used to predict the worst scenario of the onset of the crack propagation in the case when the radius of the crack tip is zero. Of course, the tip radius of real cracks is never zero, and consequently, the critical loads for real cracks are higher than the critical loads for idealized mathematical cracks predicted by Griffith. In this sense, the error induced by the classical theories generates the safety factor, which is good for engineering. In other words, we can say that the Griffith theory gives the lower bound for the critical loads.

The analysis described previously for Mode I cracks has been performed for Mode II cracks by P. Trapper and K. Y. Volokh (to appear in Engineering Fracture Mechanics). Results for Mode II cracks led to the same conclusions as described previously for Mode I cracks.

Moreover, similar computations were performed in [34] for Mode I cracks in rubber where the Neo-Hookean material model had been used:

$$\psi = \Phi - \Phi \exp\left[-\frac{\alpha}{2\Phi}(I_1 - 3)\right] \tag{4.10}$$

$$\boldsymbol{\sigma} = -p\mathbf{1} + \alpha\mathbf{B} \exp\left[-\frac{\alpha}{2\Phi}(I_1 - 3)\right] \tag{4.11}$$

where α and Φ are the shear modulus and the failure energy, respectively.

It was observed in computations based on Eqs. (4.10) and (4.11) that lower magnitudes of the critical tension were driven by (1) sharper cracks, (2) lengthier cracks, and (3) lower brittleness, that is, the ratio of the shear modulus to the failure energy. Factors 1 and 2 directly echo the classical theories of brittle fracture [33]. Factor 3 is more specific to soft materials undergoing large deformations. Simulations of the straight cracks show that the critical tension depends approximately inversely on the square root of the crack length in full harmony with the Griffith theory. Unfortunately, that is true only for the equivalent cracks, that is, cracks with the same tips. Observations of the role of the material brittleness strongly suggest that the decrease of the shear modulus as compared to the failure energy leads to a decline of the material sensitivity to a cracklike flow. This means, specifically, that the dependence of the critical load on the crack length and sharpness is less pronounced in softer materials than in more brittle ones. The latter happens because softer materials can undergo large deformations, suppressing the stress-strain concentration. In other words, softer materials absorb the high stresses and strains at the tip of the crack due to large deformations. To avoid confusion, however, we strongly emphasize

that though softer materials are less sensitive to the crack length and sharpness, they tear under lower critical loads than more brittle materials do. The latter point should not be overlooked.

Remark 4.1. Modeling fracture we assumed that the crack starts with a massive bond rupture in the process zone at the tip of the crack. This event is volumetric, and the use of the softening hyperelasticity is reasonable, unless the localized deformation and failure occur at the length scale of the material structure (grains, atomic spacing, etc.). In the latter case, the size of the finite elements cannot be decreased beyond the characteristic length of material. This limitation would introduce the characteristic length in analysis implicitly.

5. RATE-DEPENDENT FAILURE WITH ENERGY LIMITERS[1]

In this section, we examine applications of energy limiters to rate-dependent material behavior of the standard solid (Fig. 14).

In the case of small deformations, we define the viscoelastic constitutive law in the form

$$\boldsymbol{\sigma}(t)=\frac{\partial\hat{\psi}(\boldsymbol{\varepsilon})}{\partial\boldsymbol{\varepsilon}}\mathbf{1}+\int_{-\infty}^{t} m(t-\tau)\frac{\partial}{\partial\tau}\left[\mathrm{dev}\frac{\partial\bar{\psi}(\mathbf{e}(\tau))}{\partial\mathbf{e}}\right]d\tau \quad (5.1)$$

where $\varepsilon = \mathrm{tr}\boldsymbol{\varepsilon}$; $\mathbf{e} = \mathrm{dev}\,\boldsymbol{\varepsilon} \equiv \boldsymbol{\varepsilon} - (\varepsilon/3)\mathbf{1}$ and $\boldsymbol{\varepsilon}$ is the symmetric part of the displacement gradient.

The relaxation function is defined in the form

$$m\,(t-\tau) = \beta_\infty + \beta\exp\left(\frac{-(t-\tau)}{\theta}\right) \quad (5.2)$$

where $\beta_\infty = E_\infty/(E_\infty + E)$ and $\beta = E/(E_\infty + E)$ are dimensionless relative moduli and $\theta = \eta/E$ is the relaxation time.

The elastic potential is decomposed into the volumetric and distortional parts, accordingly:

$$\psi(\boldsymbol{\varepsilon}) = \hat{\psi}(\varepsilon) + \bar{\psi}(\mathbf{e}) \quad (5.3)$$

$$\hat{\psi}(\varepsilon) = \Phi_1 - \Phi_1\left(1+\sqrt{\frac{K}{\Phi_1}}\varepsilon\right)\exp\left[-\sqrt{\frac{K}{\Phi_1}}\varepsilon\right] \quad (5.4)$$

$$\bar{\psi}(\mathbf{e}) = \Phi_2 - \Phi_2\exp\left[-\frac{\mu}{\Phi_2}\,\mathbf{e}:\mathbf{e}\right] \quad (5.5)$$

[1] This and the next section include only a brief review of the results, which will be published separately elsewhere

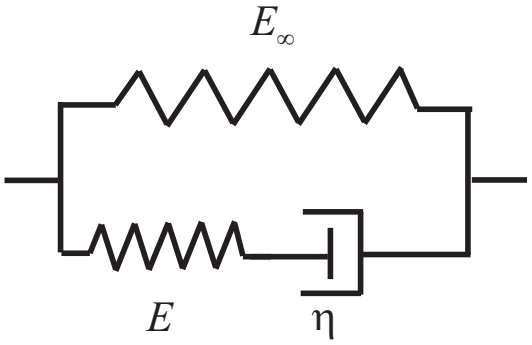

FIGURE 14. Rheological model of the standard solid

where K and μ are the bulk and shear moduli of the isotropic Hookean solid and Φ_1 and Φ_2 are the failure energies for volumetric and distortional deformations. By introducing different failure constants, we increase the flexibility of the phenomenological description of material failure.

The rate-dependent response of the model described previously in the case of simple shear is

$$\sigma_{12}(t) = 2\mu\int_0^t\left[\beta_\infty + \beta\exp\left(-\frac{t-\tau}{\theta}\right)\right] \times\frac{\partial}{\partial\tau}\left[e_{12}\exp\left(-\frac{\mu}{\Phi_2}e_{12}^2\right)\right]d\tau \quad (5.6)$$

where there is no stressing until $t = 0$.

Further simplifications are due to the assumption of the constant stretch-strain rate $\dot{\gamma} = \text{const}$. The latter assumption leads to the following simple formulae for time: $t = e_{12}/\dot{\gamma}$, $\tau = \xi_{12}/\dot{\gamma}$, where $\xi_{12} = e_{12}(\tau)$, and consequently, Eq. (5.6) takes the form

$$\sigma_{12}(t) = 2\mu\int_0^{e_{12}}\left[\beta_\infty+\beta\exp\left(-\frac{e_{12}-\xi_{12}}{\theta\dot{\gamma}}\right)\right] \times\frac{\partial}{\partial\xi_{12}}\left[\xi_{12}\exp\left(-\frac{\mu}{\Phi_2}\xi_{12}^2\right)\right]d\xi_{12} \quad (5.7)$$

Stress-strain curves defined by Eq. (5.7) are presented in Fig. 15 for different strain rates.

We use the rheological model shown in Fig. 14 as a prototype for the nonlinear model, too. The springs should be considered nonlinear in this case. We directly extend Eq. (5.1) to finite deformations

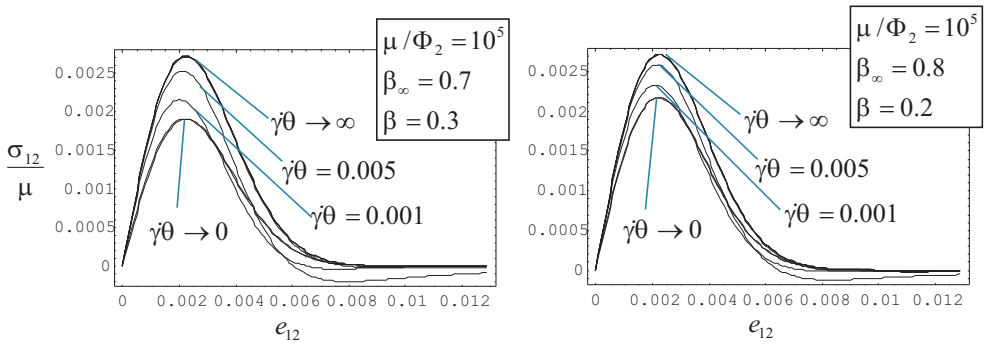

FIGURE 15. Simple shear for various strain rates

$$\boldsymbol{\tau}(t) = J\frac{\partial\hat{\psi}(\varepsilon)}{\partial\varepsilon}\mathbf{1} + \int_{-\infty}^{t} m(t-\tau)\frac{\partial}{\partial\tau} \times \left[\mathrm{dev}\left[2\bar{\mathbf{F}}(\tau)\frac{\partial\bar{\psi}(\bar{\mathbf{C}}(\tau))}{\partial\bar{\mathbf{C}}}\bar{\mathbf{F}}^{T}(\tau)\right]\right] d\tau \tag{5.8}$$

$$\boldsymbol{\sigma}(t) = \boldsymbol{\tau}(t) = -p\mathbf{1} + \int_{-\infty}^{t} m(t-\tau)\frac{\partial}{\partial\tau} \times \left\{\mathrm{dev}\left[2\mathbf{F}(\tau)\frac{\partial\psi(\mathbf{C}(\tau))}{\partial\mathbf{C}}\mathbf{F}^{T}(\tau)\right]\right\} d\tau \tag{5.10}$$

where $\boldsymbol{\tau} = J\,\boldsymbol{\sigma}$ is the so-called Kirchhoff stress tensor, $\varepsilon = J = \det\mathbf{F}$, $\bar{\mathbf{F}} = J^{-1/3}\mathbf{F}(\det\bar{\mathbf{F}} = 1)$, and $\bar{\mathbf{C}} = \bar{\mathbf{F}}^{T}\bar{\mathbf{F}}$.

The stored energy is also decomposed analogously to Eq. (5.2):

$$\psi(\mathbf{C}) = \hat{\psi}(\varepsilon) + \bar{\psi}(\bar{\mathbf{C}}) \tag{5.9}$$

Though the preceding formulation is the most general, the majority of soft materials undergoing finite deformations are incompressible. The latter means that the analytical formulation can be simplified as follows: $\varepsilon = J = \det\mathbf{F} = 1$, $\bar{\mathbf{F}} = \mathbf{F}$; $\bar{\mathbf{C}} = \mathbf{C}$; $\psi(\mathbf{C}) = \bar{\psi}(\bar{\mathbf{C}})$ and where the indefinite Lagrange multiplier, p, is used to enforce the incompressibility condition.

We further use a stored energy with softening that was calibrated for analysis of the material of AAA (Eq. (3.1)). Analogously to the previous example of small deformations, we can calculate the viscoelastic response in uniaxial tension (Fig. 16).

Evidently, the material stiffness and strength—the curve maximum—increase with the increasing deformation rate for a given relaxation time in cases of both small (Fig. 15) and large (Fig. 16) strains. This conclusion is expected intuitively. Moreover, the stable (prior to failure) branches of the response curves are limited by the curve corresponding to $\dot{\gamma}\theta \to 0$ from the bottom and $\dot{\gamma}\theta \to \infty$ from the top. Physically, the limit cases correspond to the very

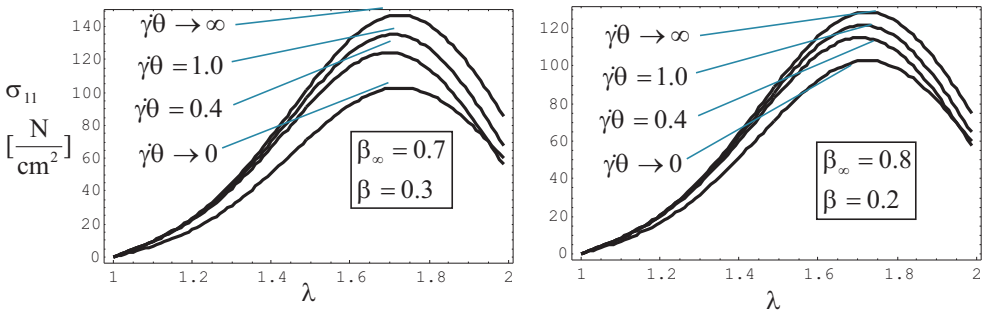

FIGURE 16. Uniaxial tension of viscoelastic AAA material for various strain rates

slow quasistatic response and the fastest instantaneous response of the material accordingly. Interestingly, the range of the strength variation depends on the relative contribution of the elastic springs in the rheological model shown in Fig. 14. The greater is the contribution of the spring corresponding to the dashpot, the larger is the strength range.

Though we used essentially different material models in the considered examples of small and finite deformations, the qualitative results are very similar. Particularly, we observed that the increasing rate of deformations leads to the increase in both stiffness and strength of the material. Such a conclusion corresponds well with the experimental observations. Moreover, while the existing viscoelasticity theories can describe the phenomenon of the material stiffening under the increasing deformation rate, the presented approach, probably for the first time, clearly predicts the increase of the material strength (and not only stiffening) with the increase of the deformation rate.

6. FLUIDS WITH FINITE STRENGTH

In this section, we use constitutive equations with softening to interpret experiments with water [36] that exhibit transition to turbulence at Reynolds numbers lower than predicted by the linear stability analysis (the subcritical transition to turbulence). To explain these observations qualitatively, we suggest that the onset of subcritical instability is related to the decline of viscosity of water: Friction between fluid layers fails with the increase of the velocity gradient. Simply speaking, the faster a fluid layer travels with respect to the adjacent layer (after some limit), the lower is the friction between them. To describe the decline of friction theoretically, we relax the assumption of the stability of the fluid material and introduce a constant of the fluid strength. Particularly, we enhance the Navier-Stokes model with a failure description by introducing the fluid strength in the constitutive equation for the viscous stress. The classical model is obtained from the enhanced one when the strength goes to infinity.

Momentum balance has the following form in the absence of body forces:

$$\rho\frac{\partial \mathbf{v}}{\partial t} + \rho\mathbf{v}\cdot\nabla\mathbf{v} = \mathrm{div}\boldsymbol{\sigma} \tag{6.1}$$

where ρ is a constant mass density, $\mathbf{v}$ is a particle velocity, t is time, and ∇ and div are the gradient and divergence operators with respect to spatial coordinates.

In the case of incompressible fluid, the Cauchy stress can be specified as follows:

$$\boldsymbol{\sigma} = -p\mathbf{1} + \boldsymbol{\tau} \tag{6.2}$$

$$\mathrm{div}\,\mathbf{v} = 0 \tag{6.3}$$

where p is the Lagrange multiplier enforcing the incompressibility Eq. (6.3); and $\boldsymbol{\tau}$ is the so-called viscous stress.

Traditionally, the constitutive model for the viscous stress in Newtonian fluids is set as follows [37, 38]:

$$\boldsymbol{\tau} = 2\eta\mathbf{D} \tag{6.4}$$

where $\eta > 0$ is a viscosity coefficient and

$$\mathbf{D} = \frac{1}{2}(\nabla\mathbf{v} + \nabla\mathbf{v}^T) \tag{6.5}$$

is a symmetric part of the velocity gradient.

Instead of Eq. (6.4), however, we will use the following constitutive model, enforcing failure or viscous and frictional bonds:

$$\boldsymbol{\tau} = 2\eta\,\mathbf{D}\exp\left[-\frac{\varepsilon^2}{\Phi^2}\right] \tag{6.6}$$

$$\varepsilon^2 = \mathbf{D}:\mathbf{D} \tag{6.7}$$

where $\varepsilon \geq 0$ is a scalar measure of the velocity gradient (the equivalent velocity gradient) and $\Phi > 0$ is a constant of fluid strength, that is, the maximum velocity gradient that preserves friction between the adjacent fluid layers.

There are two main modes for Eq. (6.6):

$$\boldsymbol{\tau} = 2\eta\mathbf{D} \quad \text{when} \quad \varepsilon \ll \Phi \tag{6.8}$$

$$\boldsymbol{\tau} = \mathbf{0} \quad \text{when} \quad \varepsilon \gg \Phi \tag{6.9}$$

The first mode, Eq. (6.8), corresponds to the classical Navier-Stokes viscosity with the full internal friction, while the second mode, Eq. (6.9), corresponds to the loss of viscosity or internal friction. These two modes reflect on Landau's remark that "for the large eddies which are the basis of any turbulent flow, the viscosity is unimportant" ([37], Section 33).

In the case of the shear flow, $\mathbf{D} = D_{12}(\mathbf{e}_1\otimes\mathbf{e}_2 + \mathbf{e}_2\otimes\mathbf{e}_1)$ and $\boldsymbol{\tau} = \tau_{12}(\mathbf{e}_1\otimes\mathbf{e}_2+\mathbf{e}_2\otimes\mathbf{e}_1)$, the constitutive law can be presented graphically (Fig. 17).

At points $D_{12}/\Phi = \pm 1/2$, the viscous strength is reached: $\tau^{\max}/\eta\Phi = \pm\exp(-1/2)$. After these points, the decline of viscosity starts. The classical Navier-Stokes theory is obtained from the modified constitutive law when the fluid strength goes to infinity: $\Phi \to \infty$.

To examine the linear stability of the flow, we superimpose small motions on the existing ones and designate the perturbations with tildes. Varying Eqs. (6.1)–(6.3) and (6.6), we have, accordingly,

$$\rho\frac{\partial\tilde{\mathbf{v}}}{\partial t} + \rho(\mathbf{v}\cdot\nabla)\tilde{\mathbf{v}} + \rho(\tilde{\mathbf{v}}\cdot\nabla)\mathbf{v} = \mathrm{div}\tilde{\boldsymbol{\sigma}} \tag{6.10}$$

$$\tilde{\boldsymbol{\sigma}} = -\tilde{p}\mathbf{1} + \tilde{\boldsymbol{\tau}}, \quad \mathrm{div}\tilde{\mathbf{v}} = 0 \tag{6.11}$$

$$\tilde{\boldsymbol{\tau}} = 2\eta\left(\tilde{\mathbf{D}} - 2\mathbf{D}\frac{\mathbf{D}:\tilde{\mathbf{D}}}{\Phi^2}\right)\exp\left[-\frac{\mathbf{D}:\mathbf{D}}{\Phi^2}\right] \tag{6.12}$$

The addition of the initial and boundary conditions of zero velocity perturbations completes the linearized Initial Boundary Value Problem (IBVP).

Let us consider stability of the Plane Couette flow (see also [39, 40] for a review). We assume that there is no pressure gradient and that the velocity field has the form $\mathbf{v} = v_1(x_2)\,\mathbf{e}_1$, where $\mathbf{e}_1$ is a unit base vector (Fig. 18). In this case, we have

$$\mathbf{D} = D_{12}(\mathbf{e}_1\otimes\mathbf{e}_2 + \mathbf{e}_2\otimes\mathbf{e}_1), \quad D_{12} = \frac{\partial v_1}{\partial x_2} \tag{6.13}$$

$$\varepsilon^2 = 2\left(\frac{\partial v_1}{\partial x_2}\right)^2 \tag{6.14}$$

$$\begin{aligned}\boldsymbol{\tau} &= \tau_{12}(\mathbf{e}_1\otimes\mathbf{e}_2 + \mathbf{e}_2\otimes\mathbf{e}_1)\\ \tau_{12} &= 2\eta\frac{\partial v_1}{\partial x_2}\exp\left[-\frac{\varepsilon^2}{\Phi^2}\right]\end{aligned} \tag{6.15}$$

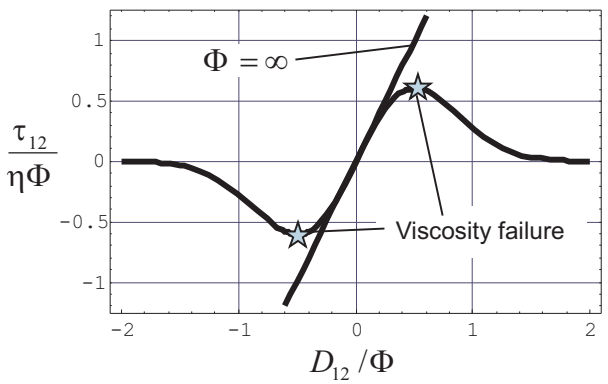

FIGURE 17. Viscous stress versus deformation rate in the case of shear flow with finite and infinite strength

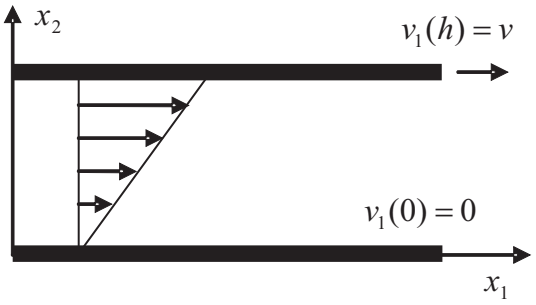

FIGURE 18. Flow between parallel plates

and the reduced momentum balance Eq. (6.1) takes the form

$$\frac{\partial\tau_{12}}{\partial x_2} = 0 \tag{6.16}$$

Substituting Eq. (6.15) into Eq. (6.16) and adding boundary conditions $v_1(0) = 0$ and $v_1(h) = v$, we find the following solution for velocity and stress fields:

$$\begin{aligned}&v_1 = \frac{vx_2}{h}, \quad \sigma_{11} = \sigma_{22} = \sigma_{33} = -p\\ &\sigma_{12} = \sigma_{21} = \frac{\eta\, v}{h}\exp\left[-\frac{2v^2}{h^2\Phi^2}\right]\end{aligned} \tag{6.17}$$

Let us study the linear stability of the obtained solution. We assume that $\tilde{p} = 0$ and $\tilde{\mathbf{v}} = \tilde{v}_1(x_2)\,\mathbf{e}_1$. Then we have

$$\tilde{\mathbf{D}} = \frac{\partial\tilde{v}_1}{\partial x_2}(\mathbf{e}_1\otimes\mathbf{e}_2 + \mathbf{e}_2\otimes\mathbf{e}_1) \tag{6.18}$$

$$\tilde{\boldsymbol{\sigma}} = \tilde{\boldsymbol{\tau}} = \beta\frac{\partial\tilde{v}_1}{\partial x_2}(\mathbf{e}_1\otimes\mathbf{e}_2 + \mathbf{e}_2\otimes\mathbf{e}_1) \tag{6.19}$$

$$\beta = 2\eta\left(1 - \frac{4v^2}{\Phi^2\,h^2}\right)\exp\left[-\frac{2\,v^2}{\Phi^2\,h^2}\right] \tag{6.20}$$

The momentum balance Eq. (6.10) reduces to

$$\rho\frac{\partial\tilde{v}_1}{\partial t} = \beta\frac{\partial^2\tilde{v}_1}{\partial x_2^2} \tag{6.21}$$

We further assume the following modes of the perturbed motion:

$$\begin{aligned}&\tilde{v}_1(x_2,t) = \text{constant}\cdot e^{\omega t}\sin(2\pi n\,x_2/h)\\ &n = 1, 2\ldots\end{aligned} \tag{6.22}$$

where boundary conditions are obeyed ($\tilde{v}_1(x_2 = 1,\, h) = 0$) and ω is a real constant.

Substituting Eqs. (6.20) and (6.22) into Eq. (6.21), we find

$$\omega = -\frac{8\eta\pi^2 n^2}{\rho h^2}\left(1 - \frac{4\,v^2}{\Phi^2\,h^2}\right)\exp\left[-\frac{2\,v^2}{\Phi^2\,h^2}\right] \quad (6.23)$$

The Couette flow is stable when ω is negative, and it loses stability when $\omega = 0$. The latter condition gives the critical velocity

$$v_c = \frac{h\Phi}{2} \quad (6.24)$$

and the critical Reynolds number

$$R_c = \frac{h\rho v_c}{\eta} = \frac{\rho h^2 \Phi}{2\eta} \quad (6.25)$$

It is interesting that in the case of the classical Navier-Stokes model, where the fluid strength is infinite, $\Phi \to \infty$, the flow is always stable with respect to the lateral perturbations (see also [41]), while in the case where strength is finite, the flow can lose stability, initiating the transition to turbulence.

Thus we found that the flow could lose its stability under the lateral velocity perturbations in the case where the fluid strength was finite. Our theoretical conclusions are in good qualitative agreement with the experimental observations on the onset of the subcritical transition to turbulence reviewed recently in [36]. It is especially interesting that the localized turbulence patterns were observed in experiments, which could be theoretically interpreted as a local loss of internal friction due to the fluctuations in the fluid strength.

7. CONCLUSIONS

In the present work, we considered novel methods for modeling material failure based on the introduction of energy limiters and/or softening in the constitutive description of solids and fluids.

The proposed methods are dramatically simpler than the existing methods of continuum damage mechanics, for example, which are traditionally used for modeling bulk failure (Table 1). The comparison given in Table 1 does not need comment, except for the following: It is necessary to be cautious in using the energy limiters in dynamic problems for *solids* where a returning wave of deformation can lead to the restoration (or healing) of the failed material. To prevent such healing, it is necessary to drop the failed elements from the finite element meshes providing the full energy dissipation. In the case of fluids, the healing is natural and should not be avoided.

TABLE 1. Comparison of continuum damage mechanics and the methods of energy limiters

	Damage internal variables	Damage threshold condition	Damage evolution equation
Damage mechanics	Yes	Yes	Yes
Energy limiters	No	No	No

We strongly emphasize, however, that the proposed approach is not a universal substitute for continuum damage mechanics. Materials exhibiting essential structural changes during deformation, for example, plasticity, creep, or fatigue, are beyond the scope of the methods of energy limiters,[2] which do not describe the structural changes in materials except for complete failure as a result of the bond rupture. The latter means, for example, that the Mullins effect in rubber, which is related to loading-unloading cycles and exhibiting material softening due to the partial structural changes or damage, is not accounted for in the present formulation with the energy limiters.

REFERENCES

1. Barenblatt, G. I., The Formation of Equilibrium Cracks during Brittle Fracture. General Ideas and Hypotheses: Axially-Symmetric Cracks. *J. Appl. Math. Mech.* **23**:622–636, 1959.
2. Dugdale, D. S., Yielding of Steel Sheets Containing Slits. *J. Mech. Phys. Solids* **8**:100–104, 1960.
3. Rice, J. R., and Wang, J. S., Embrittlement of Interfaces by Solute Segregation. *Mater. Sci. Eng. A* **107**:23–40, 1989.

[2] At least, this is true for the formulations considered in this article

4. Tvergaard, V., and Hutchinson, J. W., The Relation between Crack Growth Resistance and Fracture Process Parameters in Elastic-Plastic Solids. *J. Mech. Phys. Solids* **40**:1377–1397, 1992.
5. Xu, X. P., and Needleman, A., Numerical Simulations of Fast Crack Growth in Brittle Solids, *J. Mech. Phys. Solids* **42**:1397–1434, 1994.
6. Camacho, G. T., and Ortiz, M., Computational Modeling of Impact Damage in Brittle Materials. I. *J. Solids Struct*. **33**:2899–2938, 1996.
7. Needleman, A., A Continuum Model for Void Nucleation by Inclusion Debonding. *J. Appl. Mech*. **54**:525–531, 1987.
8. De Borst, R., Some Recent Issues in Computational Failure Mechanics. *Int. J. Numer. Meth. Eng*. **52**:63–95, 2001.
9. Belytschko, T., Moes, N., Usiu, S., and Parimi, C., Arbitrary Discontinuities in Finite Elements. *Int. J. Num. Meth. Eng*. **50**:993–1013, 2001.
10. Kachanov, L. M., Time of the Rupture Process under Creep Conditions. *Izvestiia Akademii Nauk SSSR, Otdelenie Teckhnicheskikh Nauk.* **8**:26–31, 1958.
11. Rabotnov, Y. N., On the Equations of State for Creep. In *Progress in Applied Mechanics*. Praeger Anniversary Volume. Macmillan, New York, 1963.
12. Kachanov, L. M., *Introduction to Continuum Damage Mechanics*. Martinus Nijhoff, Dortrecht, 1986.
13. Krajcinovic, D., *Damage Mechanics*. North Holland Series in Applied Mathematics and Mechanics. Elsevier, New York, 1996.
14. Skrzypek, J., and Ganczarski, A., *Modeling of Material Damage and Failure of Structures*. Springer, Berlin, 1999.
15. Lemaitre, J., and Desmorat, R., *Engineering Damage Mechanics: Ductile, Creep, Fatigue and Brittle Failures*. Springer, Berlin, 2005.
16. Gao, H., and Klein, P., Numerical Simulation of Crack Growth in an Isotropic Solid with Randomized Internal Cohesive Bonds. *J. Mech. Phys. Solids.* **46**:187–218, 1998.
17. Klein, P., and Gao, H., Crack Nucleation and Growth as Strain Localization in a Virtual-Bond Continuum. *Eng. Fract. Mech*. **61**:21–48, 1998.
18. Volokh, K. Y., Nonlinear Elasticity for Modeling Fracture of Isotropic Brittle Solids. *J. Appl. Mech*. **71**:141–143, 2004.
19. Volokh, K. Y., Softening Hyperelasticity for Modeling Material Failure: Analysis of Cavitation in Hydrostatic Tension. *Int. J. Solids Struct*. **44**:5043-5055, 2007.
20. Volokh, K. Y., Hyperelasticity with Softening for Modeling Materials Failure. *J. Mech. Phys. Solids* **55**:2237–2264, 2007.
21. Weiner, J. H., *Statistical Mechanics of Elasticity*. John Wiley, New York, 1983.
22. Tadmor, E. B., Ortiz, M., and Phillips, R., Quasicontinuum Analysis of Defects in Solids. *Philos. Mag*. **73**:1529–1563, 1996.
23. Klein, P., and Gao, H., Study of Crack Dynamics using the Virtual Internal Bond Method. In *Multiscale Deformation and Fracture in Materials and Structures*. Kluwer, Dordrecht, 275–309, 2000.
24. Volokh, K. Y., and Vorp, D. A., A Model of Growth and Rupture of Abdominal Aortic Aneurysm. *J. Biomech*. **41**:1015–1021, 2008.
25. Raghavan, M. L., and Vorp, D. A., Toward a Biomechanical Tool to Evaluate Rupture Potential of Abdominal Aortic Aneurysm: Identification of a Finite Strain Constitutive Model and Evaluation of its Applicability. *J. Biomech*. **33**:475–482, 2000.
26. Volokh, K. Y., Fung's Arterial Model Enhanced with a Failure Description. *Mol. Cell. Biomech*. **5**:207–216, 2008.
27. Vaishnav, R. N., Young, J. T., and Patel, D. J., Distribution of Stresses and of Strain-Energy Density through the Wall Thickness in a Canine Aortic Segment. *Cir. Res*. **32**:577–583, 1973.
28. Rachev, A., and Greenwald, S. E., Residual Stresses in Conduit Arteries. *J. Biomech*. **36**:661–670, 2003.
29. Volokh, K. Y., Stresses in Growing Soft Tissues. *Acta Biomater*. **2**:493–504, 2006.
30. Fung, Y. C., *Biomechanics: Motion, Flow, Stress, and Growth*. Springer, New York, 1990.
31. Fung, Y. C., *Biomechanics: Mechanical Properties of Living Tissues*, 2nd ed. Springer, New York,

1993.

32. Volokh, K. Y., Prediction of Arterial Failure Based on a Microstructural Bi-Layer Fiber-Matrix Model with Softening. *J. Biomech*. **41**:447–453, 2008.
33. Volokh, K. Y., and Trapper, P., Fracture Toughness from the Standpoint of Softening Hyperelasticity. *J. Mech. Phys. Solids* **56**:2459–2472, 2008.
34. Trapper, P., and Volokh, K. Y., Cracks in rubber. *Int. J. Solids Struct*. **45**:6034–6044, 2008.
35. Griffith, A. A., The Phenomena of Rupture and Flow in Solids. *Philos. Trans. R. Soc. London, Ser. A* **221**:163–198, 1921.
36. Mullin, T., and Kerswell, R. R., Eds. *Laminar Turbulent Transition and Finite Amplitude Solutions, Proceedings of the UITAM Symposium, Bristol, UK*. Springer, Dordrecht, 2005.
37. Landau, L. D., and Lifshitz, E. M., *Fluid Mechanics*. Pergamon Press, Oxford, UK, 1987.
38. Batchelor, G. K., *An Introduction to Fluid Dynamics*. Cambridge University Press, New York, 2000.
39. Drazin, P. G., *Introduction to Hydrodynamic Stability*. Cambridge University Press, New York, 2002.
40. Schmid, P. J., and Henningson, D. S., *Stability and Transition in Shear Flows*. Springer, New York, 2001.
41. Romanov, V. A., Stability of Plane-Parallel Couette Flow. *Funct. Anal. Appl*. **7**:137–146, 1973.